OPEN ACCESS
Journal of Innovative Optical Health Sciences
Vol. 17, No. 2 (2024) 2350021 (14 pages)

DOI: 10.1142/S1793545823500219

World Scientific
www.worldscientific.com

# Estimation-free spatial-domain image reconstruction of structured illumination microscopy

Xiaoyan Li*, Shijie Tu*, Yile Sun*, Yubing Han*,§, Xiang Hao*, Cuifang Kuang*,†,‡,¶ and Xu Liu*

*State Key Laboratory of Extreme Photonics and Instrumentation
College of Optical Science and Engineering, Zhejiang University
Hangzhou 310027, P. R. China

†ZJU-Hangzhou Global Scientific and Technological Innovation Center
Hangzhou 311200, P. R. China

‡Collaborative Innovation Center of Extreme Optics, Shanxi University
Taiyuan, Shanxi 030006, P. R. China

§Advanced Biomedical Imaging Facility-Wuhan National Laboratory for Optoelectronics, Huazhong University of Science and Technology
Wuhan, Hubei 430074, P. R. China

¶cfkuang@zju.edu.cn

Received 12 June 2023
Revised 28 June 2023
Accepted 29 June 2023
Published 18 August 2023

Structured illumination microscopy (SIM) achieves super-resolution (SR) by modulating the high-frequency information of the sample into the passband of the optical system and subsequent image reconstruction. The traditional Wiener-filtering-based reconstruction algorithm operates in the Fourier domain, it requires prior knowledge of the sinusoidal illumination patterns which makes the time-consuming procedure of parameter estimation to raw datasets necessary, besides, the parameter estimation is sensitive to noise or aberration-induced pattern distortion which leads to reconstruction artifacts. Here, we propose a spatial-domain image reconstruction method that does not require parameter estimation but calculates patterns from raw datasets, and a reconstructed image can be obtained just by calculating the spatial covariance of differential calculated patterns and differential filtered datasets (the notch filtering operation is performed to the raw datasets for attenuating and compensating the optical transfer function (OTF)). Experiments on reconstructing raw datasets including nonbiological, biological, and simulated samples demonstrate that our method has SR capability, high reconstruction speed, and high robustness to aberration and noise.

*Keywords*: Structured illumination microscopy; image reconstruction; spatial domain; digital micromirror device (DMD).

¶Corresponding author.

## 1. Introduction

In the field of super-resolution (SR) microscopic imaging of living cells, structured illumination microscopy (SIM)[1] is favored by biological and medical researchers compared to stimulated emission depletion (STED)[2] microscopy and single molecule localization microscopy (SMLM)[3–5] because of its fast image acquisition, low photobleaching effect and phototoxicity, and compatibility with general fluorescent labeling protocols.

Compared to STED and SMLM, SIM is a technology that relies on computational processing of the acquired raw datasets to reconstruct an SR image. Traditional linear two-dimensional- (2D) SIM and three-dimensional- (3D) SIM[6,7] uses nine (three orientations of 0°, 60°, and 120°, and three phases with $2\pi/3$ phase difference per orientation) and fifteen (three orientations of 0°, 60°, and 120°, and five phases with $2\pi/5$ phase difference per orientation) sinusoidal illumination patterns to acquire nine and fifteen raw measurements, respectively, for reconstruction. Processing Wiener-filtering-based reconstruction algorithm on the raw measurements, the frequency support of the system's optical transfer function (OTF) can be extended up to two times in the Fourier domain, and thus the highest 2-fold resolution enhancement can be achieved in the spatial domain. To be specific, the reconstruction process includes the separation of the high-frequency component from the low-frequency ones, position correction of the high-frequency components, and the final Wiener deconvolution. Thereinto, the first two processing steps require accurate knowledge of illumination patterns (that are spatial frequency vector, initial phase, and modulation depth these three parameters in fact) which makes parameter estimation on the raw measurements necessary. Until now, many algorithms (mainly focusing on spatial frequency vector[8,9] and initial phase[10–12]) have been proposed to estimate parameters as precisely as possible, even though, the estimation is susceptible to aberrations, noise, or experimental errors, which cause obvious artifacts in the reconstructed SIM image. For example, the estimation of the spatial frequency vector parameter will be disturbed when there are periodic structures in the sample. Besides, the estimation of the initial phase parameter is very sensitive to noise, so the estimated value may have serious deviations from the real one when the signal-to-noise ratio (SNR) of the raw measurements is low. In addition, when the biological sample is thick, aberrations introduced by the refractive index difference inside the sample itself will distort sinusoidal patterns and thus the illumination modulation will deviate from sinusoidal distribution.

In addition to the low robustness of the parameter estimation mentioned above, their time-consuming computation process is another big problem. Although the computation can be speeded up by applying the graphics processing unit (GPU)[13–15] acceleration technology, the parallel computing characteristic of GPU calls for higher configuration requirements for a computer. To solve the time-consuming problem fundamentally, some methods without parameter estimation have been proposed, and they can be divided into two types according to whether it is incompatible with the traditional SIM implementation or not. The former applies non-sinusoidal structured illumination, for example, instant SIM[16] applies multi-spot illumination to obtain an initial resolution-enhanced ($\sqrt{2}$-fold) image using optical means, and a final resolution-doubled image is produced by a subsequent deconvolution operation. The optical device[17] it relies on to get the initial image is different from the traditional SIM devices that use physical grating,[1] liquid crystal on silicon spatial light modulator (LCoS-SLM),[18] or digital micromirror device (DMD)[19–23] as projection or diffractive element to produce structure illumination. Because of the specialty and complexity of the device, the applications of instant SIM are extremely limited. Also applying multi-spot (and/or random speckle) illumination, PE-SIMS[24] obtains a resolution-doubled SIM image by calculating the spatial covariance of raw measurements and estimated patterns (obtained from an iterative calculation, and the covariance of the estimated patterns is as a statistical prior during reconstruction). The method has high robustness to aberration-induced pattern distortion and parameter tuning because of the needless parameter estimation. Nevertheless, its reconstruction process does not fully release the high-speed advantage of spatial-domain-related (SD) reconstruction due to the iterative process of pattern estimation, and because random speckle and/or multi-spot illumination patterns are needed, the device it relied on for data acquisition is limited to projection-type SIM devices. The latter applies the same implementation (nine sinusoidal illumination patterns in 2D-SIM for

example) and devices as traditional SIM, and their frameworks can be classified as SD reconstruction.[25] Among them, SDR-SIM[26] and JSFR-SIM[27–29] are two methods that still need the help of parameter estimation to construct coefficient matrixes in advance, it is because they are still linear reconstruction processes like the Wiener-filtering-based reconstruction process substantially. Differently, SPSIM[30] is a nonlinear SD reconstruction method that achieves reconstruction just by calculating the variance of raw measurements, and the reconstruction of fluorescent nanoparticles demonstrates its effective SR ability. However, because only variance is calculated, the high-frequency information of the sample may be decreased which is harmful in imaging biological samples with fine structures. On the basis of SPSIM, direct-SIM[31] considers the widefield component and adds post-processing of spectrum optimization, and the testing experiments on reconstructing nonbiological and biological samples reveal the doubled resolution enhancement and artifacts-free results, except for the additional spectrum-optimization time. To complete reconstruction entirely in the spatial domain so as to achieve a fast reconstruction speed, a method adopting a remodulation mechanism of calculating spatial covariance of measurements and illumination patterns to reconstruct a SIM image has been proposed recently.[32] It achieves one-step reconstruction in the spatial domain without the need for post-processing but only pre-processing of filtering operation on the raw measurements and deconvolution operation on the illumination patterns (captured using a mirror sample by the camera). The experiments on biological and simulated samples show high-speed and high-quality SIM reconstructions, however, its requirement of a dismountable filter before the camera in the device for the capture of the illumination patterns sets a limitation to its applications.

Here, we propose a parameter-estimation-free SD method (termed EFSD-SIM) that adopts remodulation mechanism for SIM reconstruction. In our method, we first performed notch filtering (for OTF attenuation and OTF compensation) and Wiener filtering (to calculate patterns) on the raw measurements, and then a reconstructed result could be obtained just by calculating the spatial covariance of the filtered measurements and the calculated patterns. The device that our method relies on for the acquisition of the raw measurements is compatible with the common SIM devices whether these are projection- or interference-type. Based on our home-built two-color interferometric DMD-SIM device, we acquired raw measurements of nonbiological and biological fluorescence samples for SIM reconstruction. The reconstructed results demonstrate that our method enables SR, high-speed, and artifact-free reconstruction.

## 2. Materials and Methods

### 2.1. *Theoretical analysis*

Before introducing our method, we would like to explain SIM reconstruction and resolution enhancement from the perspective of the spatial domain.

In traditional 2D-SIM, the $\ell$th measurement $M_\ell(\mathbf{r})$ is the product of the sample's fluorescence distribution $\rho(\mathbf{r})$ with the $\ell$th sinusoidal illumination patterns $I_\ell(\mathbf{r})$ and then convolved with the system's detection-side point spread function (PSF) $h_{\mathrm{det}}(\mathbf{r})$, just as follows:

$$M_\ell(\mathbf{r}) = [\rho(\mathbf{r}) \cdot I_\ell(\mathbf{r})] \otimes h_{\mathrm{det}}(\mathbf{r}), \tag{1}$$

where $\mathbf{r} = (x, y)$ denotes the lateral spatial coordinates and $\otimes$ is the convolution operator. The $\ell$th sinusoidal illumination patterns $I_\ell(\mathbf{r})$ can be given by

$$I_\ell(\mathbf{r}) = 1 + m\cos(\mathbf{k}_0\mathbf{r} - \varphi_\ell), \tag{2}$$

where $m$, $\mathbf{k}_0$, and $\varphi_\ell$ are the modulation depth, spatial frequency vector, and initial phase of the sinusoidal illumination patterns, respectively. It can be expanded as follows:

$$I_\ell(\mathbf{r}) = 1 + m\cos\varphi_\ell\cos(\mathbf{k}_0\mathbf{r}) + m\sin\varphi_\ell\sin(\mathbf{k}_0\mathbf{r}), \tag{3}$$

substituting Eq. (3) into Eq. (1), we have

$$\begin{aligned} M_\ell(\mathbf{r}) &= \rho(\mathbf{r})\otimes h_{\mathrm{det}}(\mathbf{r}) + m\cos\varphi_\ell M_c(\mathbf{r}) + m\sin\varphi_\ell M_s(\mathbf{r}) \\ &= M_0(\mathbf{r}) + m\sqrt{M_c^2(\mathbf{r}) + M_s^2(\mathbf{r})}\cos(\varphi_\ell - \theta(\mathbf{r})), \end{aligned} \tag{4}$$

where $\theta(\mathbf{r}) = \arctan(M_s(\mathbf{r})/M_c(\mathbf{r}))$, the unmodulated item $M_0(\mathbf{r}) = \rho(\mathbf{r}) \otimes h_{\mathrm{det}}(\mathbf{r})$ results from the zero-frequency component of the sinusoidal illumination patterns, $M_c(\mathbf{r}) = [\rho(\mathbf{r})\cos(\mathbf{k}_0\mathbf{r})] \otimes h_{\mathrm{det}}(\mathbf{r})$ and $M_s(\mathbf{r}) = [\rho(\mathbf{r})\sin(\mathbf{k}_0\mathbf{r})] \otimes h_{\mathrm{det}}(\mathbf{r})$ results from two high-frequency components, that are $\cos(\mathbf{k}_0\mathbf{r})$ and $\sin(\mathbf{k}_0\mathbf{r})$ of the sinusoidal illumination patterns.

If we construct a formula $\sqrt{M_c^2(\mathbf{r}) + M_s^2(\mathbf{r})}\cos(\mathbf{k}_0\mathbf{r} - \theta(\mathbf{r}))$, a reconstruction result $M_{\text{rec}}(\mathbf{r})$ can be written as follows:

$$\begin{aligned} M_{\text{rec}}(\mathbf{r}) &= M_0(\mathbf{r}) + m\sqrt{M_c^2(\mathbf{r}) + M_s^2(\mathbf{r})}\cos(\mathbf{k}_0\mathbf{r} - \theta(\mathbf{r})), \\ &= M_0(\mathbf{r}) + \frac{m}{2}\sqrt{M_c^2(\mathbf{r}) + M_s^2(\mathbf{r})} \\ &\quad \times [\exp(i(\mathbf{k}_0\mathbf{r} - \theta(\mathbf{r}))) + \exp(-i(\mathbf{k}_0\mathbf{r} - \theta(\mathbf{r})))], \\ &= M_0(\mathbf{r}) + \frac{m}{2}\{[M_c(\mathbf{r}) - iM_s(\mathbf{r})]\exp(i\mathbf{k}_0\mathbf{r}) \\ &\quad + [M_c(\mathbf{r}) + iM_s(\mathbf{r})]\exp(-i\mathbf{k}_0\mathbf{r})\}, \end{aligned} \tag{5}$$

where $M_0(\mathbf{r})$ contains sample's low-frequency component which is equivalent to a widefield image, $M_c(\mathbf{r})$ and $M_s(\mathbf{r})$ contain sample's high-frequency components which correspond to the fine structure of the sample. Therein,

$$\begin{aligned} &\sqrt{M_c^2(\mathbf{r}) + M_s^2(\mathbf{r})}\cos(\mathbf{k}_0\mathbf{r} - \theta(\mathbf{r})) \\ &= \frac{1}{2}[M_c(\mathbf{r}) - iM_s(\mathbf{r})]\exp(i\mathbf{k}_0\mathbf{r}) \\ &\quad + \frac{1}{2}[M_c(\mathbf{r}) + iM_s(\mathbf{r})]\exp(-i\mathbf{k}_0\mathbf{r}) \\ &= \frac{1}{2}\mathcal{F}^{-1}\{\tilde{\rho}(\mathbf{k})[\tilde{h}_{\text{det}}(\mathbf{k} - \mathbf{k}_0) + \tilde{h}_{\text{det}}(\mathbf{k} + \mathbf{k}_0)]\}, \end{aligned} \tag{6}$$

where $\mathcal{F}^{-1}$ denotes the inverse Fourier transform operation, $\tilde{\cdot}$ denotes the Fourier transform of a certain function, and $\tilde{h}_{\text{det}}(\mathbf{k})$ is the system's detection-side OTF with cutoff frequency $k_c$. Therefore, $M_{\text{rec}}(\mathbf{r})$ refers to an SR image with an effective OTF $[\tilde{h}_{\text{det}}(\mathbf{k} - \mathbf{k}_0) + \tilde{h}_{\text{det}}(\mathbf{k} + \mathbf{k}_0)]$ whose cutoff frequency is $k_c + |\mathbf{k}_0|$, and when the value of $|\mathbf{k}_0|$ is equal to $k_c$, the frequency support of the effective OTF can be extended 2-fold, and thus the resolution of the reconstructed SIM image can be improved by a factor of two. Besides, from Eqs. (5) and (6), we can conclude that the resolution enhancement is related to $[M_{\text{rec}}(\mathbf{r}) - M_0(\mathbf{r})]$. The principle of resolution enhancement of our method is just based on the above theory. In the following section, we give a detailed description of our method.

## 2.2. *Method*

### 2.2.1. *OTF attenuation and OTF compensation (step 1a)*

The workflow of our method is summarized in Figure 1. Empirically, the out-of-focus background originating from the "missing cone" of the OTF will give rise to significant background fluorescence and periodic honeycomb artifacts in the

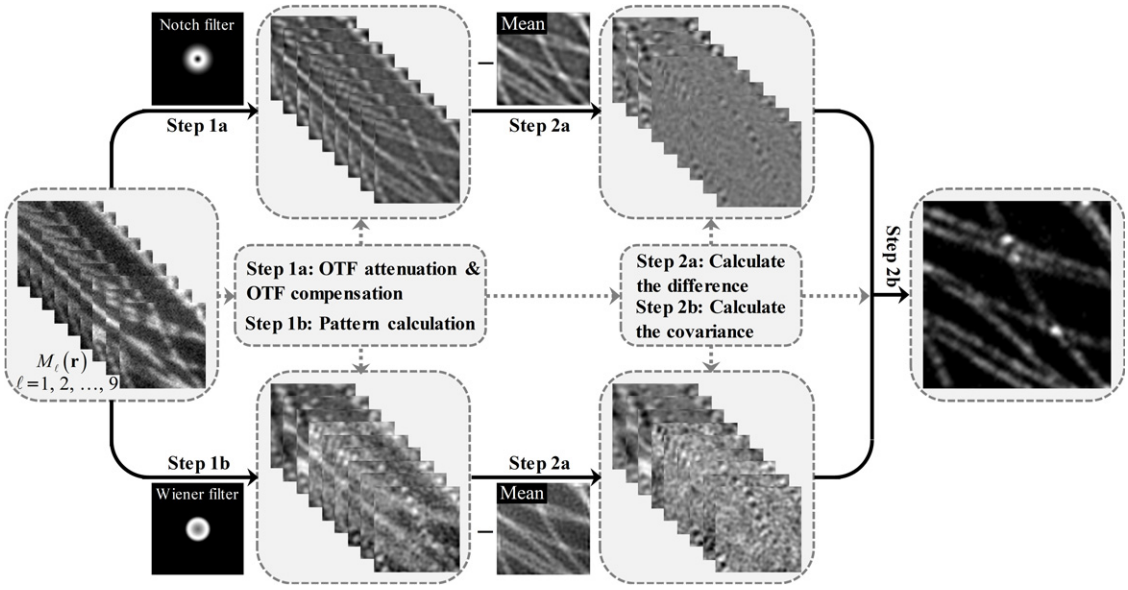


Fig. 1. Overview of the working flow of our method. The captured nine raw measurements by the camera are operated by a notch filter for OTF attenuation and OTF compensation (step 1a), and the calculated patterns are obtained from the raw measurements by applying Wiener filtering (step 1b). Then, the filtered measurements and the calculated patterns are both processed by step 2a to get their respective difference images, and a SR image is finally obtained by calculating the covariance of the two differential images in step 2b.

reconstructed result. Therefore, OTF attenuation and OTF compensation are always essential in SIM reconstruction which can be achieved by performing a bandpass notch filtering operation to the raw measurements.[27] The notch filter $\tilde{W}_{\text{notch}}(\mathbf{k})$ used in our method is as follows:

$$\tilde{W}_{\text{notch}}(\mathbf{k}) = \left[1 - a_{\text{att}} \exp\left(-\frac{\mathbf{k}^2}{2k_\sigma^2}\right)\right] \tilde{h}^*_{\text{det}}(\mathbf{k}), \quad (7)$$

where $*$ stands for conjugate operation, $a_{\text{att}}$ and $k_\sigma$ are attenuation amplitude and attenuation width, respectively, which can be adjusted empirically to get a better signal-to-background ratio according to the sample. $a_{\text{att}}$ is employed to adjust the optical sectioning performance of our method. For fluorescence samples with low out-of-focus backgrounds, the value of $a_{\text{att}}$ is generally set to zero to turn off the OTF attenuation. For fluorescence samples with strong out-of-focus backgrounds, $a_{\text{att}}$ is generally set to 0.9–1 to suppress them effectively. $k_\sigma$ is designed to adjust the area of the attenuation function, a small value of $k_\sigma$ will result in an abundant residual background, while a large value will remove most of the low-frequency components of the sample. We set $a_{\text{att}} = 1$ and $k_\sigma = 1$ in our experiments. As a result, the $\ell$th filtered measurement $M'_\ell(\mathbf{r})$ becomes

$$M'_\ell(\mathbf{r}) = \mathcal{F}^{-1}\{\tilde{M}_\ell(\mathbf{k})\tilde{W}_{\text{notch}}(\mathbf{k})\}, \quad (8)$$

its effective OTF is $\tilde{h}'_{\text{det}}(\mathbf{k}) = [\tilde{h}_{\text{det}} \cdot \tilde{W}_{\text{notch}}](\mathbf{k})$ whose cutoff frequency is consistent with that of $\tilde{h}_{\text{det}}(\mathbf{k})$.

### 2.2.2. *Pattern calculation* (*step 1b*)

Our method applies the remodulation mechanism in Ref. 30 but is different from its method of obtaining illumination patterns with a mirror sample. Instead, we get calculated patterns from the raw measurements. Because the widefield image $M_0(\mathbf{r})$ represents the convolution of the sample $\rho(\mathbf{r})$ with $h_{\text{det}}(\mathbf{r})$, the deconvoluted widefield image can be considered as the estimated low-resolution sample, just as follows:

$$M_{\text{est}-\text{sample}}(\mathbf{r}) = \mathcal{F}^{-1}\left\{\frac{\tilde{M}_0(\mathbf{k})\tilde{h}^*_{\text{det}}(\mathbf{k})}{|\tilde{h}_{\text{det}}(\mathbf{k})|^2 + \alpha}\right\}, \quad (9)$$

where $\alpha$ is Wiener constant. Similarly, From Eq. (1) we know, $M_\ell(\mathbf{r})$ represents the convolution of the $[\rho(\mathbf{r}) \cdot I_\ell(\mathbf{r})]$ with $h_{\text{det}}(\mathbf{r})$, we can perform deconvolution operation to each raw measurement to get the estimated $[\rho(\mathbf{r}) \cdot I_\ell(\mathbf{r})]$ as follows:

$$M_{\text{est}\ell}(\mathbf{r}) = \mathcal{F}^{-1}\left\{\frac{\tilde{M}_\ell(\mathbf{k})\tilde{h}^*_{\text{det}}(\mathbf{k})}{|\tilde{h}_{\text{det}}(\mathbf{k})|^2 + \beta}\right\}, \quad (10)$$

where $\beta$ is Wiener constant. With them, we calculate the $\ell$th pattern as follows:

$$\begin{aligned} P_{\text{cal}\ell}(\mathbf{r}) &= \frac{M_{\text{est}\ell}(\mathbf{r})}{M_{\text{est}-\text{sample}}(\mathbf{r}) + \sigma} \\ &= \begin{cases} 1 + m\cos(\mathbf{k}_0\mathbf{r} - \varphi_\ell), & \rho(\mathbf{r}) \neq 0, \\ 0, & \rho(\mathbf{r}) = 0, \end{cases} \end{aligned} \quad (11)$$

where $\sigma$ is a constant to guarantee the divisor is positive and $P_{\text{cal}0}(\mathbf{r}) = 1$. Besides, too-small values of Wiener constants $\alpha$ and $\beta$ will cause hammer stroke artifacts because the high-frequency noise cannot be suppressed effectively, and we set the value of both of $\alpha = 0.5$ and $\beta = 0.5$ in our experiments.

### 2.2.3. *Calculate the difference* (*step 2a*)

We have known that the resolution enhancement is related to $[M_{\text{rec}}(\mathbf{r}) - M_0(\mathbf{r})]$. Besides, from Eqs. (3)–(6) we know that it is patterns' high-frequency components rather than the zero-frequency components that shift sample's high-frequency information into the frequency support of the OTF (that is, the modulation process). Therefore, we perform differential calculations on the filtered measurements as well as the calculated patterns in our method as follows:

$$M_{\ell-\text{diff}}(\mathbf{r}) = M'_\ell(\mathbf{r}) - M'_0(\mathbf{r}), \quad (12)$$

$$P_{\text{cal}\ell-\text{diff}}(\mathbf{r}) = P_{\text{cal}\ell}(\mathbf{r}) - P_{\text{cal}0}(\mathbf{r}). \quad (13)$$

### 2.2.4. *Calculate the covariance* (*step 2b*)

The remodulation mechanism of our method is to shift the high-frequency components using the estimated patterns so that the OTF support can be expanded. Therefore, the final step of our method is to calculate the spatial covariance of the $M_{\text{diff}}(\mathbf{r})$ and the $P_{\text{cal}-\text{diff}}(\mathbf{r})$, and the covariance image is just the final reconstructed result. Specifically,

$$\begin{aligned} M_{\text{avg}}(\mathbf{r}) &= \langle M_{\ell-\text{diff}}(\mathbf{r}) \cdot P_{\text{est}\ell-\text{diff}}(\mathbf{r})\rangle_\ell \\ &= \langle [M'_\ell(\mathbf{r}) - M'_0(\mathbf{r})] \cdot [P_{\text{cal}\ell}(\mathbf{r}) - P_{\text{cal}0}(\mathbf{r})]\rangle_\ell \\ &= m^2\langle\{[(\rho(\mathbf{r})\cos(\mathbf{k}_0\mathbf{r} - \varphi_\ell)) \otimes h'_{\text{det}}(\mathbf{r})]\} \\ &\quad \times \cos(\mathbf{k}_0\mathbf{r} - \varphi_\ell)\rangle_\ell \end{aligned}$$

$$
\begin{aligned}
&= m^2\mathcal{F}^{-1}\left\{\left\langle \begin{array}{l}[(\exp(i\varphi_\ell)\tilde{\rho}(\mathbf{k}-\mathbf{k}_0) \\ \quad + \exp(-i\varphi_\ell)\tilde{\rho}(\mathbf{k}+\mathbf{k}_0)) \\ \quad \times \tilde{h}'_{\mathrm{det}}(\mathbf{k})] \\ \quad \otimes [\exp(i\varphi_\ell)\delta(\mathbf{k}-\mathbf{k}_0) \\ \quad + \exp(-i\varphi_\ell)\delta(\mathbf{k}+\mathbf{k}_0)]\end{array}\right\rangle_\ell\right\} \\
&= m^2\mathcal{F}^{-1}\left\{\left\langle \begin{array}{l}\exp(i2\varphi_\ell)\tilde{\rho}(\mathbf{k}-2\mathbf{k}_0) \\ \quad \times \tilde{h}'_{\mathrm{det}}(\mathbf{k}-\mathbf{k}_0) \\ \quad + \tilde{\rho}(\mathbf{k})\tilde{h}'_{\mathrm{det}}(\mathbf{k}-\mathbf{k}_0) \\ \quad + \tilde{\rho}(\mathbf{k})\tilde{h}'_{\mathrm{det}}(\mathbf{k}+\mathbf{k}_0) \\ \quad + \exp(-i2\varphi_\ell)\tilde{\rho}(\mathbf{k}+2\mathbf{k}_0) \\ \quad \times \tilde{h}'_{\mathrm{det}}(\mathbf{k}+\mathbf{k}_0)\end{array}\right\rangle_\ell\right\} \\
&= m^2\mathcal{F}^{-1}\left\{\begin{array}{l}\tilde{\rho}(\mathbf{k})(\tilde{h}'_{\mathrm{det}}(\mathbf{k}-\mathbf{k}_0)+\tilde{h}'_{\mathrm{det}}(\mathbf{k}+\mathbf{k}_0)) \\ \quad + \langle\exp(i2\varphi_\ell)\rangle_\ell\tilde{\rho}(\mathbf{k}-2\mathbf{k}_0) \\ \quad \times \tilde{h}'_{\mathrm{det}}(\mathbf{k}-\mathbf{k}_0) \\ \quad + \langle\exp(-i2\varphi_\ell)\rangle_\ell\tilde{\rho}(\mathbf{k}+2\mathbf{k}_0) \\ \quad \times \tilde{h}'_{\mathrm{det}}(\mathbf{k}+\mathbf{k}_0)\end{array}\right\},
\end{aligned}
\tag{14}
$$

where $\langle\cdot\rangle_\ell$ is the mean operation concerning $\ell$, and $\delta$ is the Dirac delta function. It is easy to know mathematically, $\langle\exp(\pm i2\varphi_\ell)\rangle_\ell = 0$ when $\varphi_\ell = \varphi_1 + (\ell-1)\boldsymbol{\pi}/N(N=2)$ or $\varphi_\ell = \varphi_1 + 2(\ell-1)\boldsymbol{\pi}/N(N\geq 3)$ in Eq. (14), where $N$ is the number of phase shifts in every orientation of the sinusoidal illumination patterns. On this condition, we have

$$
\begin{aligned}
M_{\mathrm{avg}}(\mathbf{r}) = m^2\mathcal{F}^{-1}\{\tilde{\rho}(\mathbf{k})[\tilde{h}'_{\mathrm{det}}(\mathbf{k}-\mathbf{k}_0) \\
+ \tilde{h}'_{\mathrm{det}}(\mathbf{k}+\mathbf{k}_0)]\}.
\end{aligned}
\tag{15}
$$

The uniformity of Eqs. (15) and (6) shows that $M_{\mathrm{avg}}(\mathbf{r})$ refers to an SR image with effective OTF $[\tilde{h}'_{\mathrm{det}}(\mathbf{k}-\mathbf{k}_0)+\tilde{h}'_{\mathrm{det}}(\mathbf{k}+\mathbf{k}_0)]$ whose cutoff frequency is $k_c + |\mathbf{k}_0|$.

### 2.3. *System*

Our method has high system flexibility, and all the raw measurements for reconstruction in the article are acquired by our home-built two-color interferometric DMD-SIM setup (Fig. 2(a)) which is mounted on an inverted fluorescence microscope (Ellipse Ti, Nikon).

Before the DMD, there are two modules including the wavelength switching and fiber coupling module and the laser combination module. In the

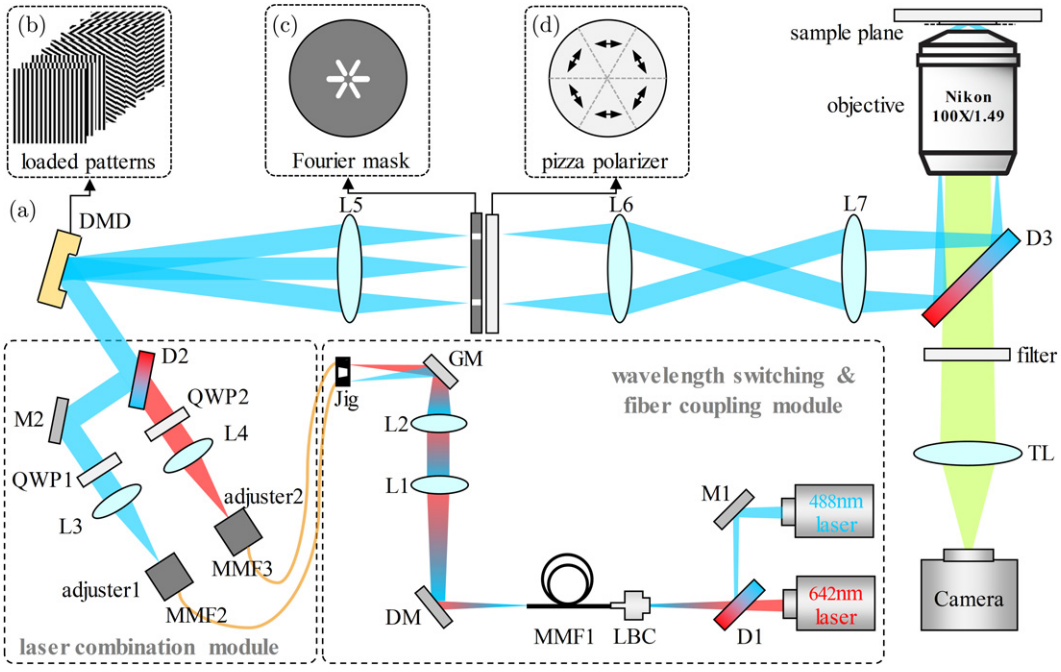


Fig. 2. The diagram of our custom-built DMD-SIM system. (a) Experimental setup. There are two modules including wavelength switching and fiber coupling module and laser combination module before the diffraction element DMD. M1 and M2, mirror; D1–D3, dichroic mirror; L1–L7, lens; LBC, laser beam coupler; MMF1–MMF3, multimode fiber; DM, deformable mirror; GM, galvanometer; QWP1-QWP2, quarter-wave plate; TL, tube lens. (b)–(d) are the binary grating patterns loaded onto the DMD, the homemade Fourier mask, and the pizza polarizer, respectively.

wavelength switching and fiber coupling module, the 642 nm laser (Red 2RU-VFL-P-642, MPB Communications) and the 488 nm laser (Blue 2RU-VFL-P-488, MPB Communications) reflected from a mirror M1 are combined with a dichroic mirror (D1, ZT488rdc, chroma), and then coupled into a customized square-core multimode fiber (MMF1, $70\,\mu\text{m} \times 70\,\mu\text{m}$, numerical aperture (NA) 0.22) using a laser beam coupler (LBC, 60SMS-1-4-RGBV11-47, Schäfter + Kirchhoff). Subsequently, the output laser beam reflected from a deformable mirror (DM, $\mu$DM, Dyoptyka) passes through a pair of lenses (L1 and L2) of 1.5-fold magnification. The high-frequency (500 kHZ) DM is used to suppress MMFs' speckle effect. Then, the laser is reflected from a galvanometer (GM, S-8107, Sunny) which could swing at different angles to switch the two laser wavelengths. The "on" laser beam of 488 nm (642 nm) is coupled into the corresponding square-core MMF2 (MMF3) (M103L05, Thorlabs, $150\,\mu\text{m} \times 150\,\mu\text{m}$, 0.39 NA) whose ceramic head of fiber's input port is fixed in the Jig. The Jig is mounted on a compact five-axis stage (PY005, Thorlabs) which is used to adjust the positions of the ceramic heads to guarantee maximum light transmission. In the laser combination module, the output ports of MMF2 and MMF3 are fixed in 2D adjuster1 and adjuster1, respectively. Then, the collimated 488 nm laser (reflected from M3) and 642 nm laser after L3 and L4 are combined with D2 (DMLP505R, Thorlabs) and arrive at the DMD. Although the two colors used in our experiment have almost the same angle of incidence (40.58° for 488 nm and 40.22° for 642 nm to DMD's base surface using micromirrors in the "on" state, their angle of reflection is the same 16.58° to the DMD base surface. The angles are calculated by the simulation method in Ref. 22 in advance) to illuminate the DMD, we separate the 488 nm and 642 nm laser light paths apart so that this design guarantees that our device can be expanded to simultaneous two-color imaging easily.

The binary grating patterns shown in Fig. 2(b) are prepared to be loaded onto the DMD, and there are three diffraction orders (0 order and ±1 order) after lens L5 (TTL200, Thorlabs). A homemade Fourier mask (Fig. 2(c)) keeps the passage at ±1 order and blocks the zero-order and orders higher than 1. The grooved hole maintains the passage of ±1 order diffracted by the grating pattern with different periods, and the width of the groove is 1 mm. The adjuster1 and adjuster2 can adjust the translation of the ±1 order in the transverse plane of the Fourier mask to ensure unblocked passage of ±1 order. Behind it, there is a customized pizza polarizer (Fig. 2(d)) consisting of six pieces of polarizing films to control the polarization of the three pairs of ±1 order beam, and every two opposite pieces have identical tangential polarization directions. Because the laser beams are circularly polarized after passing through MMFs and quarter-wave plates (QWP1 and QWP2), with the pizza polarizer, the respective ±1 order beam in every orientation becomes identical tangential polarization which guarantees the highest interference fringe contrast. The two diffracted beams finally come to the microscope objective (Nikon, 100X/1.49 TIRF) through a couple of lenses (L6 and L7, TTL200, Thorlabs) and interfere at the sample plane. The fluorescence emitted from the sample is separated from the laser by a polarization-maintaining dichroic mirror D3 (ZT405/488/561/640-phase R-UF3, Chroma) and then focused by a microscope's tube lens (TL) onto a scientific complementary metal-oxide-semiconductor (sCMOS) camera (Dhyana 400BSI V2.0, Tucsen). The exposure time of the camera was 50 milliseconds in our experiments.

## 3. Results

### 3.1. *Imaging experiment results*

To demonstrate the reconstruction performance of our method, we conducted reconstructions on raw measurements of fluorescence nanoparticles and biological fluorescence samples that are obtained by our home-built two-color interferometric DMD-SIM device. We compared the reconstructed results of our method with the SD method JSFR-SIM[27] and the high-fidelity Fourier-domain method HiFi-SIM,[33] both of which have the requirement of parameter estimation.

First, we imaged 100 nm fluorescent nanoparticles and a ground truth fluorescent calibration slide (Argo-SIM V2, Argolight) under an excitation wavelength of 488 nm, the corresponding emission wavelength is 525 nm. In the experiment, we loaded nine binary grating patterns (three orientations of 0°, 60°, and 120°, and three phases with $2\pi/3$ phase difference per orientation) with a period of 12 DMD

pixels onto the DMD, and the period of the sinusoidal illumination patterns is 339 nm. Figures 3(a) and 3(b) show the widefield image and its decorrelation analysis[34] result, and Figs. 3(c) and 3(d) show the EFSD-SIM image and its decorrelation analysis result. The bold vertical lines in Figs. 3(b) and 3(d) indicate the normalized local maximum of the highest frequency $k_{max}$ which corresponds to a

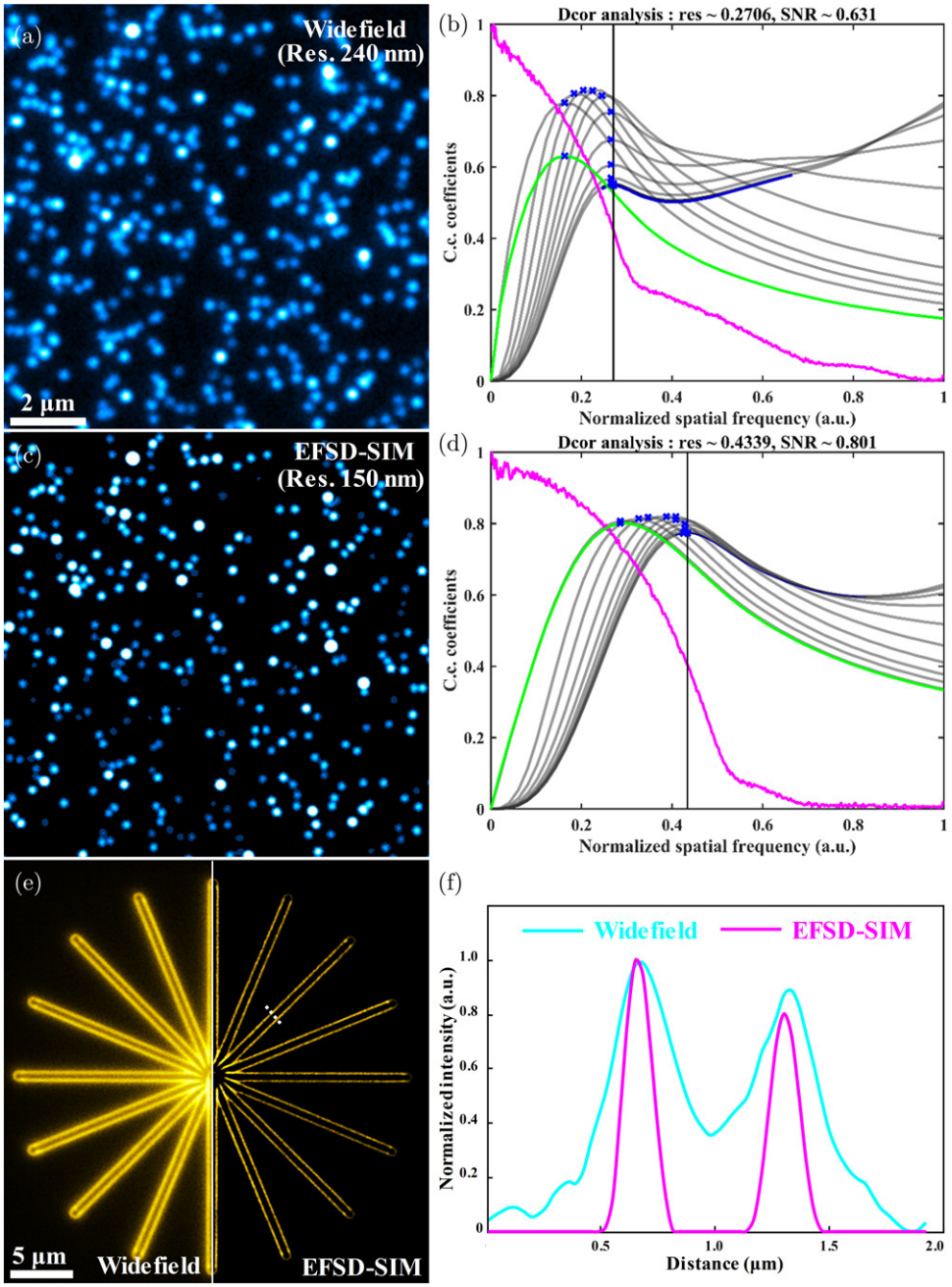


Fig. 3. Experimental results of nonbiological fluorescence samples under an excitation wavelength of 488 nm. (a) and (b) is widefield image of 100 nm nanoparticles (average of the nine raw datasets) and the result of decorrelation analysis[33] of (a) respectively. (b) and (c) are SIM images of 100 nm nanoparticles reconstructed using our method and the result of the decorrelation analysis of (b) respectively. The values of resolution in (a) and (c) are calculated as ($2 \times$ pixel size/$k_{max}$), the pixel size in (a) and (c) is 32.5 nm, the $k_{max}$ is the normalized local maximum of the highest frequency of (a) and (b), that is the "res" value as shown in the top of (b) and (d). (e) is the widefield image (left) and EFSD-SIM (right) image of star geometrical figure of fluorescent calibration slide. The normalized intensity profiles along the white line at the same position of widefield image and EFSD-SIM image in (e) is shown in (f). SNR, signal-to-noise ratio; C.c., cross-correlation.

resolution of $(2 \times \text{pixel size}/k_{\max})$, and the image pixel size in Figs. 3(a) and 3(c) is 32.5 nm. As a result, the resolution of the EFSD-SIM image is 150 nm, which is 1.6-fold higher than that of the widefield image, i.e., 240 nm, the resolution enhancement is consistent with the theoretical value of 1.63 (calculated as $1 + 215/339$, 215 is calculated by the Rayleigh criterion $0.61 \times 525/1.49$). The Argo-SIM V2 calibration slide has geometrical star with 16 arms, and Fig. 3(e) shows the widefield image and EFSD-SIM image of the star. We can see that the hollow structures of the arms are more resolvable in the EFSD-SIM image, and the difference is more visualized in the intensity profiles, as shown in Fig. 3(f).

Secondly, we imaged AF488-labeled outer membrane protein Tom-20 of mitochondria in fixed Cos-7 cells, and the reconstructed results of our method, SPSIM, JSFR-SIM, and HiFi-SIM are shown in Fig. 4(a). It shows that all the SIM images enable a clearer distinction of the mitochondrial protein distribution compared to the widefield image. The images in Fig. 4(b) are obtained by taking the Fourier transform of the corresponding images in Fig. 4(a), and the white circle indicates the boundary of the spectrum range of the HiFi-SIM image. It can be found that the spectral range of the EFSD-SIM image is wider than that of the SPSIM image and comparable to that of JSFR-SIM and HiFi-SIM images. It means that our algorithm has a comparable degree of resolution enhancement to JSFR-SIM and HiFi-SIM algorithms and does not lose high-frequency sample information compared to the SPSIM algorithm at the same time, it can be seen more obviously in Figs. 4(c) and 4(d) which are magnified regions of interest (ROIs) 1 and 2 in Fig. 4(a).

Finally, we imaged beta-tubulins (E7) stained with STAR RED dye in fixed Cos-7 cells under an excitation wavelength of 642 nm, and the emitted fluorescence wavelength is 670 nm. In the experiment, we loaded binary grating patterns with a period of 8 DMD pixels onto the DMD and thus the period of the sinusoidal illumination patterns was 290 nm. We conducted reconstructions using our method, JSFR-SIM, and HiFi-SIM, respectively, the results are shown in Fig. 5. In Figs. 5(a)–5(d), the resolutions (calculated using decorrelation

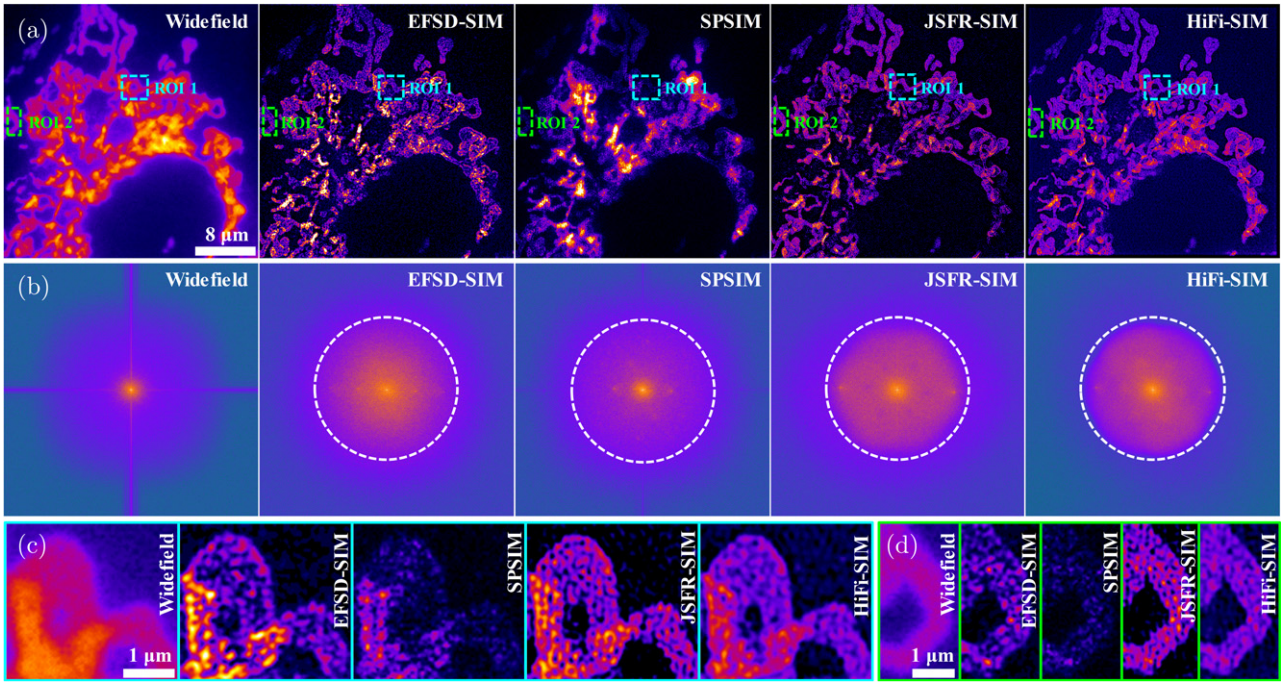


Fig. 4. Experimental results of AF488-dyed mitochondria in a fixed Cos-7 cell under an excitation wavelength of 488 nm. (a) Widefield image and SIM images reconstructed with our method, SPSIM, JSFR-SIM, and HiFi-SIM. (b) The corresponding spectral distributions (obtained by taking the Fourier transform of the corresponding images, and the white circle indicates the boundary of the spectrum range of the HiFi-SIM image) in (a). (c) and (d) are magnified images of the ROI 1 (cyan-dashed-box) and ROI 2 (green-dashed-box) in (a), respectively. ROI: Region of interest.

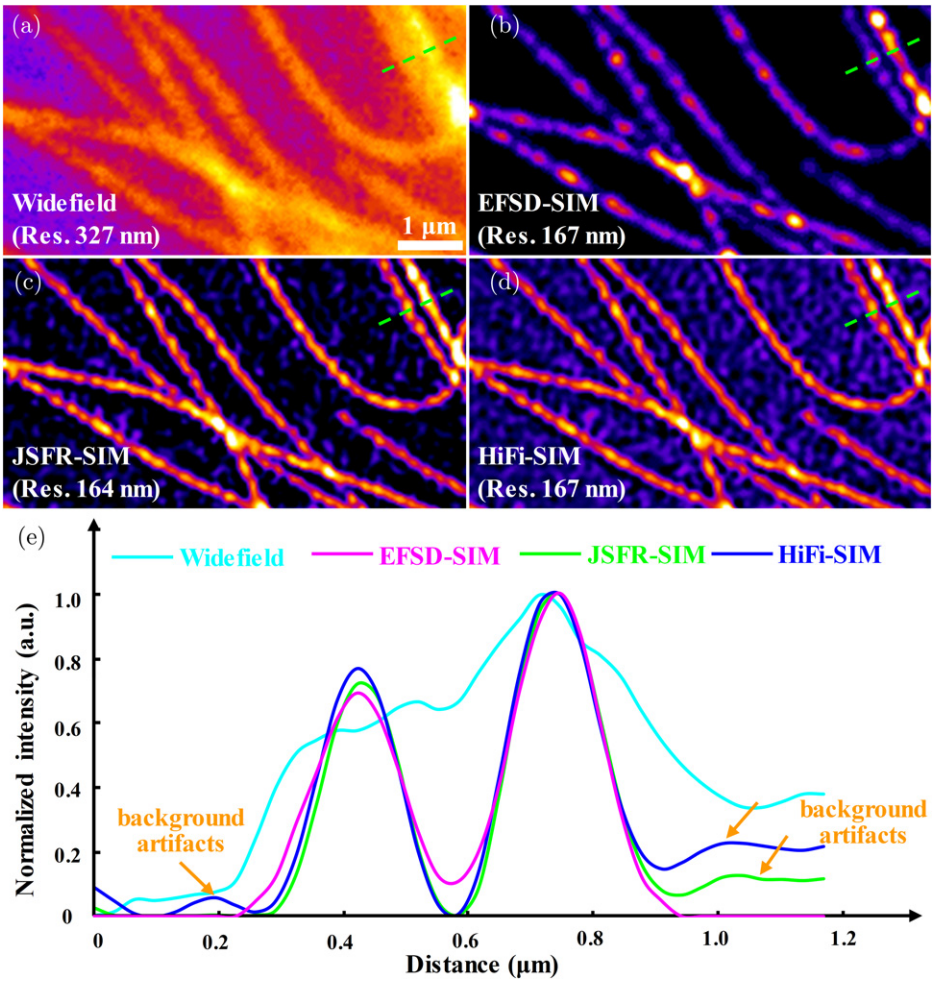


Fig. 5. Experimental results of STAR-RED-dyed microtubules in a fixed Cos7-1 cell under an excitation wavelength of 642 nm. (a) Widefield image and SIM images reconstructed with (b) our method, (c) JSFR-SIM, and (d) HiFi-SIM. Their respective resolution is calculated using decorrelation analysis algorithm. (e) Intensity profiles along the green dashed lines in (a)–(d), and all the intensity profiles are normalized to their peak intensities.

analysis algorithm) of the widefield, EFSD-SIM, JSFR-SIM, and HiFi-SIM images are 327 nm, 167 nm, 164 nm, and 167 nm, respectively. The theoretical widefield resolution is calculated by the Rayleigh criterion (274 nm; calculated as $0.61 \times 670/1.49$), and the respective 1.96-fold, 1.99-fold, and 1.96-fold resolution enhancement of EFSD-SIM, JSFR-SIM, and HiFi-SIM is consistent with the theoretical value of 1.94-fold (calculated as $1 + 274/290$). Besides, the two adjacent microtubule filaments (under the respective green dashed line in Figs. 5(a)–5(d)) which cannot be resolved in the widefield image are resolvable in the EFSD-SIM, JSFR-SIM, and HiFi-SIM images, it can be seen more intuitively from their respective intensity profiles in Fig. 5(e). Meanwhile, our method is less prone to background artifacts compared to JSFR-SIM and HiFi-SIM, as indicated by the arrows in Fig. 5(e).

### 3.2. *Simulation experiment results*

Furthermore, we quantified the resolution enhancement and robustness of our method to distortion and noise with the simulated Siemens star test target, the results are shown in Fig. 6. In the simulation experiment, we set system parameters as follows: Objective NA of 1.49, excitation wavelength of 488 nm, and emission wavelength of 525 nm, respectively. The simulated star sample (Fig. 6(a)) and its ROI (Fig. 6(b)) were both illuminated under sinusoidal illumination patterns with a period of 296 nm which corresponds to 10 pixels of our DMD. In Fig. 6(c), the widefield

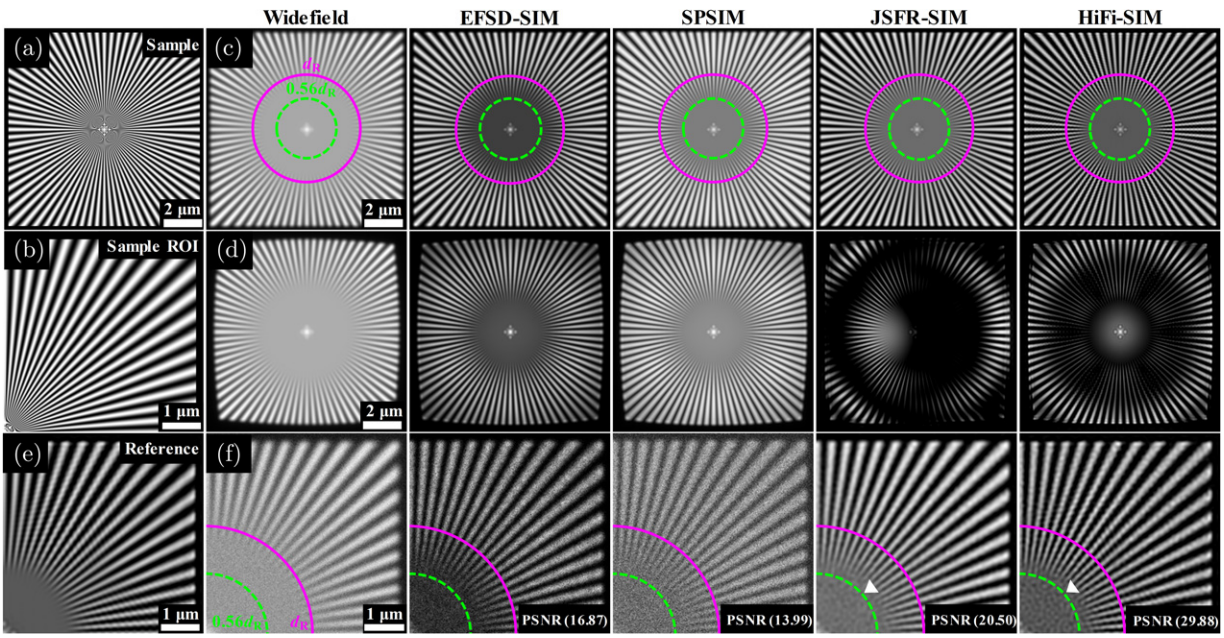


Fig. 6. Simulation experiment results. (a) and (b) is the simulated Siemens star target and its ROI, respectively. (c) and (d) are experimental results of the simulated Siemens star under a widefield microscope, our method, SPSIM, JSFR-SIM, and HiFi-SIM using nondistorted and distorted sinusoidal illumination patterns, respectively. The magenta and green curves indicate the resolutions of widefield imaging and SIM imaging, respectively, and $d_R$. is the Rayleigh criterion. (e) is the same ROI of the HiFi-SIM image in (c) as in (b), it is considered as a reference to calculate values of PSNR of (f) the EFSD-SIM, SPSIM, JSFR-SIM, and HiFi-SIM images reconstructed from nine raw measurements that are added with 25 dB Gaussian noise. PSNR: peak signal to noise.

resolution $d_R$ is the Rayleigh criterion, and the resolution of our method is $0.56d_R$ (quantified by reading the minimal resolved period when the contrast reaches 0.01). As a result, our method achieves 1.79-fold resolution enhancement which is consistent with the theoretical value of 1.73 (calculated as $1 + 215/296$), and the resolution of the EFSD-SIM image is comparable with that of the SPSIM, JSFR-SIM image and HiFi-SIM image. In addition, our method has high robustness to optical aberrations[35] and noise, as shown in Figs. 6(d)–6(f). In Fig. 6(d), the star sample was illuminated by distorted sinusoidal illumination patterns, and the reconstruction results indicate that our method provides comparable aberration-robustness to SPSIM, however, the results of JSFR-SIM and HiFi-SIM both have different degrees of deterioration. Figure 6(e) is the ROI of an ideal HiFi-SIM reconstruction image whose sinusoidal illumination patterns are absent of distortion or noise, and we considered it as a reference to calculate the respective peak signal-to-noise ratio (PSNR) of the same ROI of EFSD-SIM, SPSIM, JSFR-SIM, and HiFi-SIM images (all of them were reconstructed from nine raw measurements that were added with 25 dB Gaussian noise). As shown in Fig. 6(f), the value of PSNR of the EFSD-SIM image is 16.87, it is higher than that of the SPSIM image (13.99) and lower than that of JSFR-SIM (20.50) and HiFi-SIM (29.88) images which have obvious artifacts in the high-frequency region near the $0.56d_R$ however.

### 3.3. *Reconstruction speed testing results*

Moreover, we compared the respective reconstruction speed of our method, JSFR-SIM, and HiFi-SIM in Table 1. The methods were all executed on MATLAB 2021a based on the same workstation (Dell Precision T7610, Intel(R) Xeon(R) CPU E5-2690 v2 @ 3.0 GHz, 3.0 GHz, 20 Cores; RAM 80 GB;

Table 1. Execution time for tested methods.

| | Reconstruction time (ms) | |
|---|---|---|
| Method | CPU | GPU |
| HiFi-SIM | $5507.0 \pm 93.6$ | — |
| JSFR-SIM | $680.6 \pm 26.9$ | $11.6 \pm 2.0$ |
| Our method | $613.2 \pm 15.7$ | $28.6 \pm 0.7$ |

NVIDIA GeForce RTX 2080 Ti 11 GB). The nine raw measurements were up-sampled by a factor of two before reconstruction and the output reconstructed image size is $1024 \times 1024$, and the values shown in Table 1 are the average execution time of 10 individual processing events. The result of the comparison is that the reconstruction speed of our method is $\sim 8.98$-fold and $\sim 1.11$-fold faster than HiFi-SIM and JSFR-SIM respectively in the CPU environment, and $\sim 2.47$-fold lower than JSFR-SIM in the GPU environment.

## 4. Discussion

In fact, as a promotion, because $\langle \exp(\pm i2\varphi_\ell) \rangle_\ell = 0$ can also be achieved when $\varphi_\ell = \varphi_1 + (\ell - 1)\pi/N$( $N = 2$) in Eq. (14), in principle, our method can be extended to a more time-saving reconstruction mechanism with seven frames which include six raw measurements (three orientations of $0^\circ$, $60^\circ$, and $120^\circ$, and two phases with $\pi/2$ phase difference per orientation) and one widefield image (can be obtained by taking the average of the six raw measurements) compared to the present nine-frame reconstruction. Besides, because the remodulation mechanism of our method just relies on the frequency-spectrum-shifting characteristic of the estimated sinusoidal patterns, any illumination patterns that can be decomposed into superposition of sinusoidal functions, such as lattice and speckle, can be combined with our method in principle. Open-source codes and test data for our method are available on our GitHub repository: https://github.com/Xiaoyan-github/zjulxy.git.

## 5. Conclusions

In conclusion, we have proposed an SD-SIM reconstruction method termed EFSD-SIM without the requirement of knowing specific illumination patterns and thus the time-consuming parameter estimation procedure. What is novel, we obtain required patterns by calculating from raw measurements to achieve remodulation. The reconstruction of our method is conducted directly by calculating the spatial covariance of the differential calculated patterns and the differential filtered measurements (by performing notch filtering on the raw measurements for background suppression). We quantified the SR capability, the reconstruction speed, and the robustness to noise and pattern distortion of our method by performing reconstructions on the raw measurements of the nonbiological/biological fluorescence samples and the simulated Siemens star target. The reconstruction results show that our method provides equivalent or better performance in terms of resolution enhancement, reconstruction speed, and noise/aberration-robustness compared to the state-of-the-art methods whether with the requirement of parameter estimation (including the SD method JSFR-SIM and the Fourier-domain method HiFi-SIM) or not (the SD algorithm SPSIM). The speed advantage of our method makes it has potential to be used in the real-time imaging by applying 7-frame reconstruction in the future.

## Acknowledgments

This research was funded by the National Natural Science Foundation of China (62125504, 61827825, and 31901059), Zhejiang Provincial Ten Thousand Plan for Young Top Talents (2020R52001), Open Project Program of Wuhan National Laboratory for Optoelectronics (2021WNLOKF007).

## Conflicts of Interest

The authors declare that there are no conflicts of interest relevant to this article.

## References

1. M. G. L. Gustafsson, "Surpassing the lateral resolution limit by a factor of two using structured illumination microscopy," *J. Microsc.* **198**, 82–87 (2000).
2. S. W. Hell, J. Wichmann, "Breaking the diffraction resolution limit by stimulated emission: Stimulated-emission-depletion fluorescence microscopy," *Opt. Lett.* **19**, 780–782 (1994).
3. E. Betzig, G. H. Patterson, R. Sougrat, O. W. Lindwasser, S. Olenych, J. S. Bonifacino, M. W. Davidson, J. Lippincott-Schwartz, H. F. Hess, "Imaging intracellular fluorescent proteins at nanometer resolution," *Science* **313**, 1642–1645 (2006).
4. S. T. Hess, T. P. K. Girirajan, M. D. Mason, "Ultra-high resolution imaging by fluorescence photoactivation localization microscopy," *Biophys. J.* **91**, 4258–4272 (2006).

5. M. J. Rust, M. Bates, X. Zhuang, "Sub-diffraction-limit imaging by stochastic optical reconstruction microscopy (STORM)," *Nat. Meth.* **3**, 793–795 (2006).
6. M. G. L. Gustafsson, L. Shao, P. M. Carlton, C. J. R. Wang, I. N. Golubovskaya, W. Z. Cande, D. A. Agard, J. W. Sedat, "Three-dimensional resolution doubling in wide-field fluorescence microscopy by structured illumination," *Biophys. J.* **94**, 4957–4970 (2008).
7. L. Shao, P. Kner, E. H. Rego, M. G. L. Gustafsson, "Super-resolution 3D microscopy of live whole cells using structured illumination," *Nat. Meth.* **8**, 1044–1046 (2011).
8. S. A. Shroff, J. R. Fienup, D. R. Williams, "Phase-shift estimation in sinusoidally illuminated images for lateral superresolution," *J. Opt. Soc. Am. A* **26**, 413–424 (2009).
9. A. Lal, C. Shan, P. Xi, "Structured illumination microscopy image reconstruction algorithm," *IEEE J. Sel. Top Quant.* **22**, 6803414 (2016).
10. K. Wicker, "Non-iterative determination of pattern phase in structured illumination microscopy using auto-correlations in Fourier space," *Opt. Exp.* **21**, 24692–24701 (2013).
11. K. Wicker, O. Mandula, G. Best, R. Fiolka, R. Heintzmann, "Phase optimisation for structured illumination microscopy," *Opt. Exp.* **21**, 2032–2049 (2013).
12. R. Cao, Y. Chen, W. Liu, D. Zhu, C. Kuang, Y. Xu, X. Liu, "Inverse matrix based phase estimation algorithm for structured illumination microscopy," *Biomed. Opt. Exp.* **9**, 5037–5051 (2018).
13. A. Markwirth, M. Lachetta, V. Moenkemoeller, R. Heintzmann, W. Huebner, T. Huser, M. Mueller, "Video-rate multi-color structured illumination microscopy with simultaneous real-time reconstruction," *Nat. Commun.* **10**, 4315 (2019).
14. M. Aydin, Y. Uysalli, E. Ozgonul, B. Morova, F. Tiryaki, E. N. Firat-Karalar, B. Dogan, A. Kiraz, "An LED-based structured illumination microscope using a digital micromirror device and GPU accelerated image reconstruction," *Plos One* **17**, 0273990 (2022).
15. F. Xu, J. Zhang, D. Ding, W. Liu, C. Zheng, S. Zhou, Y. Chen, C. Kuang, "Real-time reconstruction using electro-optics modulator-based structured illumination microscopy," *Opt. Exp.* **30**, 13238–13251 (2022).
16. A. G. York, P. Chandris, D. D. Nogare, J. Head, P. Wawrzusin, R. S. Fischer, A. Chitnis, H. Shroff, "Instant super-resolution imaging in live cells and embryos via analog image processing," *Nat. Meth.* **10**, 1122–1126 (2013).
17. A. Curd, A. Cleasby, K. Makowska, A. York, H. Shroff, M. Peckham, "Construction of an instant structured illumination microscope," *Methods* **88**, 37–47 (2015).
18. H.-W. Lu-Walther, M. Kielhorn, R. Foerster, A. Jost, K. Wicker, R. Heintzmann, "fastSIM: A practical implementation of fast structured illumination microscopy," *Methods Appl. Fluoresc.* **3**, 014001 (2015).
19. D. Dan, M. Lei, B. Yao, W. Wang, M. Winterhalder, A. Zumbusch, Y. Qi, L. Xia, S. Yan, Y. Yang, P. Gao, T. Ye, W. Zhao, "DMD-based LED-illumination super-resolution and optical sectioning microscopy," *Sci. Rep.* **3**, 1116 (2013).
20. M. Li, Y. Li, W. Liu, A. Lal, S. Jiang, D. Jin, H. Yang, S. Wang, K. Zhanghao, P. Xi, "Structured illumination microscopy using digital micro-mirror device and coherent light source," *Appl. Phys. Lett.* **116**, 233702 (2020).
21. A. Sandmeyer, M. Lachetta, H. Sandmeyer, W. Huebner, T. Huser, M. Mueller, "Cost-effective live cell structured illumination microscopy with video-rate imaging," *Acs Photon.* **8**, 1639–1648 (2021).
22. P. T. Brown, R. Kruithoff, G. J. Seedorf, D. P. Shepherd, "Multicolor structured illumination microscopy and quantitative control of polychromatic light with a digital micromirror device," *Biomed. Opt. Exp.* **12**, 3700–3716 (2021).
23. X. Li, S. Xie, W. Liu, L. Jin, Y. Xu, L. Zhang, X. Hao, Y. Han, C. Kuang, X. Liu, "Speckle-free laser projection structured illumination microscopy based on a digital micromirror device," *Opt. Exp.* **29**, 43917–43928 (2021).
24. L.-H. Yeh, L. Tian, L. Waller, "Structured illumination microscopy with unknown patterns and a statistical prior," *Biomed. Opt. Exp.* **8**, 695–711 (2017).
25. P. T. C. So, H. S. Kwon, C. Y. Dong, "Resolution enhancement in standing-wave total internal reflection microscopy: a point-spread-function engineering approach," *J. Opt. Soc. Am. A* **18**, 2833–2845 (2001).
26. D. Dan, Z. Wang, X. Zhou, M. Lei, T. Zhao, J. Qian, X. Yu, S. Yan, J. Min, P. Bianco, B. Yao, "Rapid image reconstruction of structured illumination microscopy directly in the spatial domain," *IEEE Photon. J.* **13**, 3053110 (2021).
27. Z. Wang, T. Zhao, H. Hao, Y. Cai, K. Feng, X. Yun, Y. Liang, S. Wang, Y. Sun, P. R. Bianco, K. Oh, M. Lei, "High-speed image reconstruction for optically sectioned, super-resolution structured illumination microscopy," *Adv. Photon.* **4**, 026003 (2022).
28. Z. Wang, T. Zhao, Y. Cai, J. Zhang, H. Hao, Y. Liang, S. Wang, Y. Sun, T. Chen, P. R. Bianco, K. Oh, M. Lei, "Rapid, artifact-reduced, image

reconstruction for super-resolution structured illumination microscopy," *Innov.* **4**, 100425 (2023).
29. T. Zhao, Z. Wang, Y. Cai, Y. Liang, S. Wang, J. Zhang, Y. Sun, T. Chen, M. Lei, "Fast single-layer reconstruction for three-dimensional structured illumination microscopy," *Opt. Laser. Eng.* **167**, 107606 (2023).
30. S. Tu, Q. Liu, X. Liu, W. Liu, Z. Zhang, T. Luo, C. Kuang, X. Liu, X. Hao, "Fast reconstruction algorithm for structured illumination microscopy," *Opt. Lett.* **45**, 1567–1570 (2020).
31. G. Wen, Y. Liang, L. Wang, J. Zhang, X. Chen, X. Jin, C. Chen, Y. Tang, H. Li, "Spectrum-optimized direct image reconstruction of super-resolution structured illumination microscopy," *PhotoniX* **4**, 19 (2023).
32. S. Tu, X. Li, Y. Wang, W. Gong, X. Liu, Q. Liu, Y. Han, C. Kuang, X. Liu, X. Hao, "High-speed spatially re-modulated structured illumination microscopy," *Opt. Lett.* **48**, 2535–2538 (2023).
33. G. Wen, S. Li, L. Wang, X. Chen, Z. Sun, Y. Liang, X. Jin, Y. Xing, Y. Jiu, Y. Tang, H. Li, "High-fidelity structured illumination microscopy by point-spread-function engineering," *Light. Sci. Appl.* **10**, 70 (2021).
34. A. Descloux, K. S. Grussmayer, A. Radenovic, "Parameter-free image resolution estimation based on decorrelation analysis," *Nat. Meth.* **16**, 918–924 (2019).
35. X. Liu, S. Tu, Y. Xu, H. Song, W. Liu, Q. Liu, C. Kuang, X. Liu, X. Hao, "Aberrations in structured illumination microscopy: A theoretical analysis," *Front. Phys.* **7**, 00254 (2020).